RESEARCH ARTICLE

Experimentation in Exploring Photovoltaic Inverter Dynamics Under Different Irradiance Levels Through a Data-Driven Approach

BIDUR POUDEL [1,2], (Member, IEEE), NISCHAL GURUWACHARYA [2], (Member, IEEE), SUNIL SUBEDI[3], (Member, IEEE), UJJWOL TAMRAKAR [4], (Member, IEEE), FELIPE WILCHES-BERNAL [4], (Senior Member, IEEE), HOSSEIN MORADI REKABDARKOLAEE [5], (Senior Member, IEEE), TIMOTHY M. HANSEN [1], (Senior Member, IEEE), AND REINALDO TONKOSKI [6], (Senior Member, IEEE)

[1]Department of Electrical Engineering and Computer Science, South Dakota State University, Brookings, SD 57007, USA
[2]National Renewable Energy Laboratory, Golden, CO 80401, USA
[3]Oak Ridge National Laboratory, Oak Ridge, TN 37830, USA
[4]Sandia National Laboratories, Albuquerque, NM 87123, USA
[5]Mathematics and Statistics Department, South Dakota State University, Brookings, SD 57007, USA
[6]Department of Electric Power Transmission and Distribution, Technical University of Munich, 80333 Munich, Germany

Corresponding author: Bidur Poudel (bidur.poudel@jacks.sdstate.edu)

ABSTRACT As conventional direct connections of synchronous generators are being phased out, inverter-based resources (IBRs) with grid support functions are increasingly being integrated into power systems. This transition requires the development of accurate dynamic models for IBRs to predict how power systems will adapt to varying levels of IBRs penetration, establish grid code requirements, and ensure compliance. This study introduces an active probing signal-based data-driven modeling technique to accurately derive the dynamics model of a smart photovoltaic inverter operating in Volt-Watt and Freq-Watt modes, in compliance with the IEEE 1547-2018 standard. The paper focuses on investigating how the dynamics of the PV inverter model respond to fluctuations in solar irradiance, utilizing real-time digital simulator experimentation. The experimental analysis demonstrates that the amplitude of dynamics fluctuates with changes in irradiance across both operational modes and confirms the active power's dependence on irradiance levels. Furthermore, the nature of inverter dynamics varies distinctly between the different modes of activation. Critically, our findings indicate that dynamic models require DC-gain adjustments to accommodate contrasting irradiance levels, highlighting a negative gradient linear relationship between the DC-gain of each model and the irradiance.

INDEX TERMS Data-driven modeling, IEEE 1547-2018, PV inverter dynamics, real-time digital simulator, solar irradiance.

NOMENCLATURE

COTS	Commercial-Off-the-Shelf.
GOF	Goodness of Fit.
GSFs	Grid Support Functions.
IBRs	Inverter Based Resources.
NRMSE	Normalized Root-Mean-Square-Error.
PV	Photovoltaic.
PCC	Point of Common Coupling.

The associate editor coordinating the review of this manuscript and approving it for publication was Md. Rabiul Islam.

PECs   Power Electronic Converters.
RTDS   Real-Time Digital Simulator.
SysId   System Identification.
TF   Transfer Function.

I. INTRODUCTION

Inverter-based systems are becoming increasingly popular, with solar photovoltaic (PV) and wind being the most commonly used resources. However, as synchronous generators are phased out to maximize generation from these systems, the grid's stability is weakened, leading to voltage/frequency stability issues [1], [2]. To address this problem, grid support functions (GSFs) are added to inverter-based resources (IBRs) at transmission and distribution levels. Inverters equipped with GSFs such as Volt-Watt, Volt-VAr, Freq-Watt, and voltage/frequency ride-through capabilities are designed to offer voltage and frequency ancillary services under the IEEE 1547-2018 standard for IBRs [3]. Precise dynamic models of inverters are essential for grid operators, researchers, system planners, and other stakeholders to understand how the power system will function with different levels of inverter-based resource penetration and to determine grid code requirements and additional integration of inverter-based resources [4]. In addition, well-tested inverter models are required for advanced inverter-based resource controller design, optimization, supervision, fault detection, and diagnosis techniques [5]. Therefore, accurate, repeatable, and comparable experiments require precise inverter models to reduce risks in modern power systems.

Vendor-specific inverter dynamic models vary from manufacturer to manufacturer and are proprietary. This includes the physical architecture of the inverters, voltage/current control loop models, phase-locked loop (PLL) models, and GSFs standards. In power system modeling and simulation studies, employing vendor-specific models can offer advantages, particularly when aiming to incorporate equipment from a specific vendor. Yet, in broader studies where proprietary models might be inaccessible, data-driven alternatives can serve as valuable options. These models have the potential to mitigate errors and enhance the accuracy of results and analyses [6]. Inaccurate modeling, results, and analysis caused power outages in Great Britain, Australia, and Europe [7], [8]. Moreover, the intermittency of DERs and the complexity of power systems require regular updates of the dynamic models of inverters, which are not always feasible with physics-based models provided by the vendor [9]. This highlights the need for regularly updated electromagnetic transient models of grid-supportive power electronics converters (PECs).

PECs can be modeled using various techniques (e.g., switching models, linear regression models, neural networks models, wavelets models, classical models, fuzzy models, averaged linear models, dynamic phasor models, artificial neural network (ANN) [10], [11], [12], [13], [14], [15], [16], [17], [18]). The definitions, advantages, and disadvantages of each modeling technique is described in the Table 1.

An alternative is using a data-driven approach via active probing signal-based system identification (SysId) to extract the inverter's dynamics model [19]. Data-driven approaches have demonstrated remarkable abilities and have been utilized in synchronous generator parameter identification [20], aggregated load model identification [21], control design – reduced order model identification for power system stabilizer design [22], sub-synchronous resonance screening or stability analysis [23], Phasor measurement unit (PMU) based oscillation mode analysis [24], [25], etc. Few studies use data-driven approaches to inverter modeling and validate these models with power hardware-in-the-loop experiments as they provide flexibility in testing analog test beds or real systems. Our previous study [26], [27], [28], [29] extracted the dynamics model of PEC in Volt-VAr mode using active probing signal-based data-driven model parametrization. The research examines how using four different probing signals affects model parametrization and goodness-of-fit (GOF) when extracting models. However, it does not consider the PEC dynamics in Volt-Watt and Freq-Watt modes nor experimentally verify if the inverter's dynamics change with activation mode. Observations, measurements, and simulations can provide insights into the system's dynamics. In a data-driven approach, perturbing PECs with properly designed probing signals is important as it is the only method to influence the process and learn more about the behavior of the system [5], [30], [31]. However, the literature does not discuss the limitations of designing probing signals for PEC perturbation.

On the one hand, PV power generation is affected by fluctuations in solar radiation and cloud cover. The amount of power and current a PV system produces depends on various factors such as irradiance, temperature, and DC voltage [32], [33]. To control the active and reactive power of a PV system, the instantaneous capability curves of the PV generator must be taken into account, which changes with the level of irradiance, temperature, and other environmental variables [34], [35]. In addition, the control strategy and power output of a PV system can be influenced by external factors. Different modeling techniques exist, such as dynamic PV models [36], irradiance-based performance models [37], bifacial PV irradiance models [38], machine learning-based models [39], and concentrated solar power models [40]. These modeling approaches demonstrate how the level of irradiance can affect the output of individual models. However, there is a gap in the literature regarding the study of inverter dynamics and how inverter dynamic models are affected by varying levels of solar irradiance.

The main objective of this paper is to explain the process of extracting dynamic models of a COTS inverter using an experimental setup while activating the Volt-Watt and Freq-Watt modes. It also examines how the dynamics change when different GSFs are activated. Additionally, the paper discusses the design criteria for generating probing signals to perturb the COTS inverter. Finally, the paper also explores

TABLE 1. Summary of power electronic converter model type definitions, advantages, and disadvantages.

Model Types	Formulation & Level of Detail	Simulation Time-Step	Advantages	Disadvantages	References
Switched	• Detailed model • Incorporates power electronic switching components and PWM control	ns to μs	• Captures all non-linearities • Provides the highest accuracy for dynamic stability analysis	• Computationally intensive • Requires determination of numerous parameters	[13]
Dynamic Phasor	• Utilizes dynamic phasors for multi-frequency representation • Capable of integrating electromagnetic dynamics within a phasor-based framework • Allows adjustment of model order to simulate various dynamic behaviors	depends on model order	• Potentially more accurate than average and positive-sequence models • Applicable for both positive and negative sequence components	• Mathematically intricate • Challenging to apply traditional small-signal stability analysis methods	[16]
ANN	• Non-linear statistical models developed through data training • Able to capture complex patterns and non-linear relationships	depends on model and training	• Highly flexible and adaptable to diverse datasets • Effective at processing high-dimensional data and learning intricate relationships • Can generalize effectively to new data if trained appropriately	• Needs large datasets and substantial training • Susceptible to overfitting without proper regularization • Can be difficult to interpret the model	[11]
Fuzzy Model	• Rule-based system using fuzzy logic • Handles imprecision and uncertainty in data	depends on rule set complexity	• Good for systems with uncertain or vague information • Easy to incorporate expert knowledge through rule base • Effective in control applications with imprecise inputs	• Rule-based models can become complex and difficult to manage • Performance heavily depends on the quality of the rule set • Not well-suited for systems requiring precise numerical modeling	[41]
Wavelet Model	• Decomposes signals into time-frequency components • Suitable for analyzing non-stationary signals	depends on wavelet and decomposition level	• Excellent for capturing transient and non-stationary features • Can provide multi-resolution analysis of signals • Useful for fault detection and signal processing	• Computationally intensive, especially for high-resolution analysis • Requires careful selection of mother wavelet and decomposition level • Interpretation of results can be complex	[5]
Data-Driven	• Based on experimental or field input and output data • Mathematical model tailored to the data	depends on time-step of data	• Eliminates the need for prior knowledge of the converter's internal structure or parameters • Able to identify parameter degradation • Generally less computationally intensive than parameterized models	• Requires extensive data for model training • Applicable only to systems with available operational field data • May have limitations in modeling non-linear waveform dynamics • Model accuracy depends on the time-step of the collected data	[26], [28], [42]

the relation between dynamic models of the PV inverter and varying irradiance levels through real-time digital simulator (RTDS) experimentation.

The rest of the paper is organized as follows: Section II presents the modeling of the COTS inverter dynamics with GSFs. Section III presents the experimental setup for identifying the reduced order dynamic models of a two-wire single-phase inverter (SMA inverter) operating in the Volt-Watt and Freq-Watt modes. The results are shown in Section IV, and Section V concludes the study.

II. MODELING COTS INVERTER DYNAMICS WITH GSFS

This section provides an overview of GSFs from the IEEE 1547-2018 standard. It highlights the concept of partitioned modeling for extracting the non-linear dynamics of the PV inverter operating in the Volt-Watt and Freq-Watt modes. In addition, this section also explains the design criteria of the probing signal used in SysId and its algorithm. Furthermore, the process of employing SysId to develop a detailed COTS inverter dynamics model will be explained along with a flowchart to determine the transfer function (TF) of inverter dynamics.

A. OVERVIEW OF GSFs FROM IEEE 1547-2018 STANDARD

Several GSFs for IBRs are being added for supplementary voltage and frequency services [43]. This paper focuses on two different modes of operation of an inverter, namely the Volt-Watt and the Freq-Watt modes. However, the proposed method presented in this research analysis can also be extended to other GSFs of an inverter.

1) VOLTAGE-ACTIVE POWER (VOLT-WATT) FUNCTION

According to the updated IEEE 1547-2018 standard, when the Volt-Watt [4] function of an inverter becomes activated, the inverter must actively limit the maximum active power of IBRs (P_{rated}) as a function of voltage by using the linear characteristics curve of voltage-active power in parts as represented in Fig. 1. The inverter responds appropriately to the Volt-Watt characteristics curve by curtailing its active power feed-in when the grid voltage fluctuates and operates above a predetermined threshold value (V_1). However, when the grid voltage exceeds the upper limit voltage (V_2), the inverter ceases to inject active power into the grid.
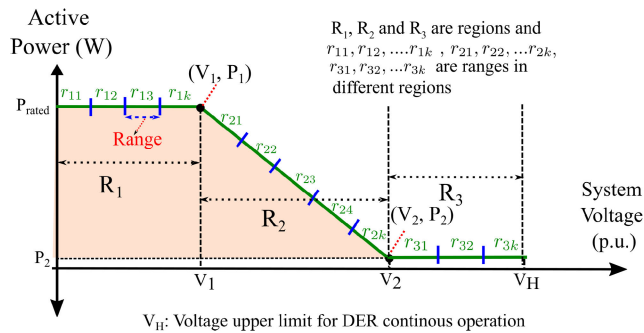

FIGURE 1. The Volt-Watt characteristics curve depicts several regions and ranges.

2) FREQUENCY-ACTIVE POWER (FREQ-WATT) FUNCTION

Like as in Volt-Watt mode, when the Freq-Watt function [4] of an inverter is activated, an inverter shall actively limit the P_{rated} of an IBRs as a function of frequency using the linear characteristics curve of frequency-active power in pieces as represented in Fig. 2. The inverter responds appropriately to the frequency-active power characteristics curve by altering its active power feed-in when the grid frequency fluctuates

and goes above a predetermined threshold (F_1) by a defined gradient. However, when the grid frequency equals the upper bound frequency (F_2), the inverter ceases to inject active power into the grid.
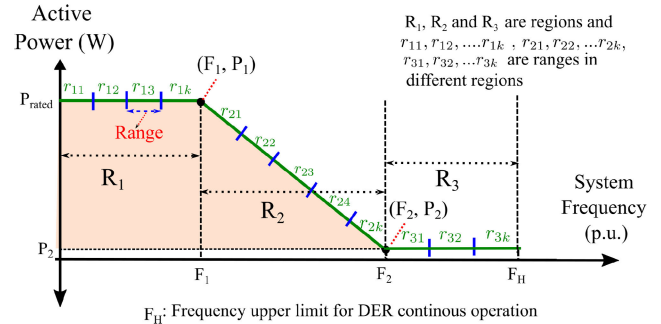

FIGURE 2. The Freq-Watt characteristics curve depicts several regions and ranges.

B. PARTITIONED MODELING OF VOLT-WATT/FREQ-WATT

The complicated dynamics of an entire operating region of a Volt-Watt/Freq-Watt mode cannot be adequately captured by a single linearized model as there are non-linearities in the PECs, leading to intricate dynamic models when modeling PECs with GSFs [42], [44]. Therefore, the complicated operating regions are split into numerous small linear areas. Based on the voltage and frequency magnitude availability, each region (represented by R) is divided into several small ranges (represented by r). Ranges are selected based on the resolution of the measurement devices. The regions and ranges of the Volt-Watt and Freq-Watt characteristics curves are shown in Fig. 1 and Fig. 2, respectively. The term r_{1k} represents the range in which the first index shows the region and the second represents voltage/frequency amplitude change, respectively.

C. DATA-DRIVEN MODEL PARAMETRIZATION USING SYSTEM IDENTIFICATION

The SysId technique determines a linear TF for each small range. SysId is obtaining a mathematical model of an unknown system based on the input and the corresponding output dataset. The input and output datasets obtained from simulation or experimentation are subdivided into training and testing datasets. The poles and zeros are varied from a second-order to a fifth-order model to create distinct linearized models that are both accurate and computationally efficient [26]. These models, characterized by their respective poles and zeros, are compared using Akaike's Final Prediction Error (AFPE), and the model with the lowest AFPE which is second order is selected as the final TF model for each range [43]. A SysId toolbox available in MATLAB [45] or a user-defined SysId algorithm can be utilized to approximate the model of an unknown system. The training datasets are used to estimate the parameters (i.e., the coefficient of a TF) of an unknown dynamic

system by minimizing a defined cost function (e.g., Least square error) [46]. The testing datasets are used to validate the obtained TF. The quantification of the performance of an unknown dynamic model is accomplished through the computation of GOF. The fit of the model can be calculated using a metric such as the normalized root-mean-square-error (NRMSE) defined as [47]:

$$\text{NRMSE} = \left(\frac{\|\hat{y}(t) - y(t)\|_2}{\sqrt{N} \left(\max(\hat{y}(t)) - \min(\hat{y}(t)) \right)} \right) \quad (1)$$

$$\text{GOF} = (1 - \text{NRMSE}) \times 100\% \quad (2)$$

where, $\|.\|_2$ represents Euclidean norm, $y(t)$ is the actual value of data considered, $\hat{y}(t)$ is the estimated value of data and N is the number of data point considered. The Flowchart for data-driven model parametrization using SysId to determine the TF of a COTS inverter operating in Volt-Watt and Freq-Watt mode is shown in Fig. 3.
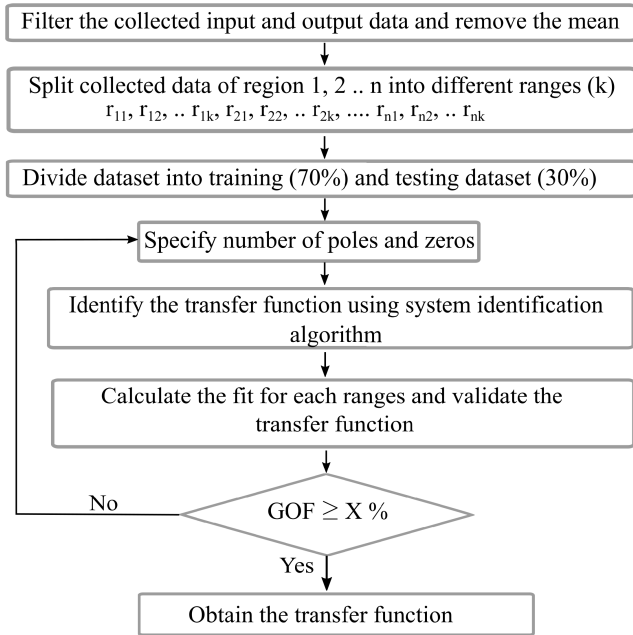

FIGURE 3. Flowchart to carry out data-driven model parametrization using SysId.

D. PROBING SIGNALS

Perturbing PECs with properly designed probing signals is essential in a data-driven model parametrization. It is the only method to influence the process and learn more about the behaviors of systems [5]. However, the design constraints imposed by the power system and the concept of positioning the content of the probing signal in the frequency band of interest need to be strictly followed while utilizing it as a perturbation signal [48].

In our previous work on deriving the dynamics model of a COTS inverter, we designed a probing signal using a console PC. This signal was then inputted into a power

amplifier simulating a grid, perturbing the PCC voltage. The inverter's response was recorded while the Volt-VAr function was active. The performance of four different probing signals, namely logarithmic square chirp, square, sine, and logarithmic sine chirp, were compared [26] and the logarithmic square chirp signal outperformed other signals when extracting dynamic models. Therefore, a logarithmic square chirp signal is used as a probing signal to perturb the system. The signal has the following fundamental notion:

$$x(t) = A \text{ square}(wt) \quad (3)$$

Here, $x(t)$ is the logarithmic square chirp signal, A is the square wave's peak amplitude, and wt is the phase, which gets updated according to the trapezoidal method indicated in the following Eqn. 4.

$$(wt)_k = (wt)_{k-1} + \frac{t_k - t_{k-1}}{2} \times 2 \times \pi \times (f_{(t_k)} + f_{(t_{k-1})}) \quad (4)$$

where $(wt)_{k-1}$ and $(wt)_k$ represent previous and current time instant phase angle, t_{k-1} and t_k are the time at discrete instant $k-1$ and k, $f_{(t_k)}$ and $f_{(t_{k-1})}$ are the frequency at t_k and t_{k-1} respectively. Similarly, the frequency $f_{(t_k)}$ is defined as in:

$$f(t_k) = f_0 \times \frac{f_0^{(\frac{1}{T})^{t_k}}}{f_1} \quad (5)$$

where f_0, f_1, and T represent the chirp signal's starting frequency, final frequency, and time length, respectively.

Algorithm 1 Probing Signal Generation
___
Input: Peak amplitude (A) of the signal based on signal-to-noise ratio
Calculate dominant system time constant (τ_{system})
Calculate final frequency (f_1) $\approx \frac{1}{2 \times T_h} \approx \frac{1}{2 \times \tau_{system}}$
Initialization:
Starting frequency (f_0) $\leftarrow \frac{f_1}{10}$
Percentage rate of exponential change of frequency $\leftarrow D\%$
if $\tau_{model} \neq \tau_{system}$ **then**
    1) Update f_0
    2) Calculate $T \leftarrow \frac{1}{D\% \times f_0 \times log(\frac{f_1}{f_0})}$
    3) Design input signal and perturb the system
    4) Collect input and output datasets
    5) Apply data-driven model parametrization using SysId algorithm
    6) Calculate time constant of derived model (τ_{model})
else
    Accept the designed probing signal and the identified model.
end

---

1) DESIGN CRITERIA OF CHIRP SIGNAL

Based on the fundamental explanation of the signal, the design criteria of the chirp signal presented in this paper are f_0, f_1, T, and A.
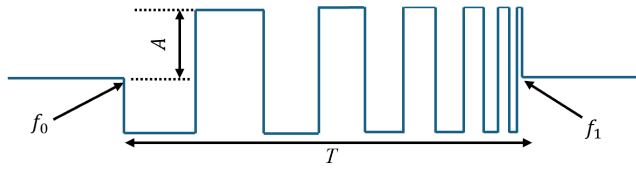
FIGURE 4. Graphical representation of logarithmic square chirp signal.

a: FINAL FREQUENCY (F_1)

The parameter f_1 is the final frequency of the chirp signal. In other words, it is the frequency at which the designed signal will have minimum hold time (T_h) (i.e., the shortest period for which the signal stays constant). However, T_h of the signal should neither be chosen too small nor too large. If it is selected too small, the process will have no time to settle, and the model identified from such data will not be able to describe the static behavior well. Similarly, if selected too large, it would overemphasize low frequencies, and the model obtained might not properly capture the process behavior as the data contains no information on them. Hence, it is reasonable to choose the minimum T_h approximately equal to the time constant (τ_{system}) of the system [5]. Hence, the final frequency of the signal can be obtained as follows:

$$f_1 \approx \frac{1}{2 \times T_h} \approx \frac{1}{2 \times \tau_{system}}$$

The multiplication of 2 in the f_1 equation is carried out to consider the signal's total ON and OFF time.

Furthermore, to determine τ_{system}, the system is given a step input and the system's settling time (t_s) is calculated. Depending on the tolerance band considered, τ_{system} can be calculated as [49], [50]:

$$\tau_{system} = \frac{t_s}{3} \quad \text{(for 5\% tolerance band)}$$

$$\tau_{system} = \frac{t_s}{4} \quad \text{(for 2\% tolerance band)}$$

b: STARTING FREQUENCY (F_0)

The minimum frequency of a chirp signal, f_0, is selected iteratively until the time constant of the predicted model (τ_{model}) matches τ_{system} as indicated in Algorithm 1.

c: TIME LENGTH OF SIGNAL (T)

The time length of the chirp signal, T, is expressed as the time between two particular instantaneous frequencies f_0 and f_1 and is expressed as [51]:

$$T = \frac{1}{D\% \times f_0 \times log(\frac{f_1}{f_0})}$$

where D is the percentage rate of exponential change in the signal frequency.

d: PEAK AMPLITUDE OF SIGNAL (A)

The peak amplitude of the logarithmic square chirp signal, A, should be chosen considering the signal-to-noise ratio [9],

which varies depending on the system. It should be carefully chosen so that the output signal incorporates the least amount of noise possible after perturbing the system with designed signals. Poor selection may necessitate using other filters to remove noise, which will be covered in more detail in the results and analysis section. The algorithm for designing the probing signal for data-driven model parametrization is given in Algorithm 1.

E. DC-GAIN OF A TRANSFER FUNCTION

DC-gain of the system is defined as the gain of the system when the frequency is zero. The DC-gain of the transfer function can be determined by comparing the given transfer function with the standard time constant form, which is represented below:

$$G(s) = \frac{K \times (1 + s\tau_1)(1 + s\tau_2)(1 + s\tau_3)\ldots\ldots(1 + s\tau_n)}{s^n(1 + s\tau_1')(1 + s\tau_2')(1 + s\tau_3')\ldots\ldots(1 + s\tau_n')}$$

Here, K is the DC-gain of the system, τ and τ' are the time constants of the system, and n is the order of the system. In another way, K can be obtained as [52]:

$$K = \lim_{s \to 0} s^n G(s). \tag{6}$$

III. EXPERIMENTAL SETUP

An RTDS experimentation setup can be used to test COTS inverters under IEEE 1547-2018 standard voltage and frequency settings. The test equipment used in this experiment is a commercial single-phase 5 kW SMA inverter, whose dynamic model will be determined when operating in Volt-Watt and Freq-Watt modes. The experimental setup to determine the dynamics of an SMA with GSFs is depicted in Fig. 5.
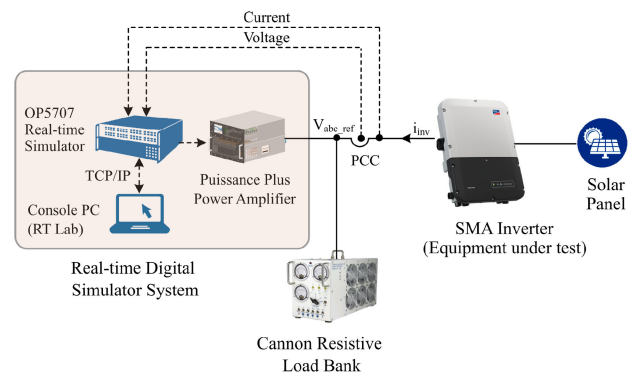

FIGURE 5. Experimental setup to determine TF of SMA operated in Volt-Watt and Freq-Watt mode. The SMA is probed through a power amplifier unit controlled through an Opal-RT RTDS.

The experimental setup consists of a rooftop PV system (23 kW), a single-phase 5 kW SMA inverter, a Puissance Plus Power Amplifier (acting as a grid), an OP5707 RTDS, a Cannon Resistive Load Bank, and a console PC. The RTDS and power amplifier, combined with a console PC, were used to perturb the voltage and frequency at the point of

common coupling (PCC). A Cannon Resistive Load Bank was connected at the PCC to utilize the PV power while protecting against reverse power flow to the power amplifier. A console PC was used to design the probing signal to perturb the voltage and frequency amplitudes at the PCC. The MATLAB/Simulink model of the probing signal was built, compiled, and loaded into the OP5707 RTDS, which was interfaced with the console PC to generate variable voltage and frequency amplitudes at the power amplifier input terminals. The console PC and RTDS communicated using the transmission control protocol/internet protocol. A power amplifier that received a small analog probing signal from the RTDS at its input terminals produced an amplified probing signal at its output terminals. The perturbed voltage and frequency amplitude in the PCC of the power amplifier, along with the current injected into the grid by the SMA, were recorded to capture the dynamics of the inverter.

To capture the dynamics of an inverter operating in either Volt-Watt or Freq-Watt mode, the corresponding modes were activated by selecting Volt-Watt or Freq-Watt settings based on the IEEE standard in the inverter. The procedure for turning on any mode in the SMA inverter is described in [53]. The logged corresponding output voltage at the PCC, the current injected from the inverter to the grid, and irradiance were passed through the RTDS system. The SysId toolbox available in MATLAB/Simulink was used to implement the SysId technique described in the previous section. The TF to be identified from the given data set is described below:

$$G(s) = \frac{\Delta Output}{\Delta Input} = \frac{b_m s^m + b_{m-1} s^{m-1} + \ldots + b_0}{a_n s^m + a_{n-1} s^{n-1} + \ldots + a_0} \quad (7)$$

The terms $b_m..b_0$, $a_n..a_0$ are the respective coefficients of the TF to be estimated from the recorded dataset.
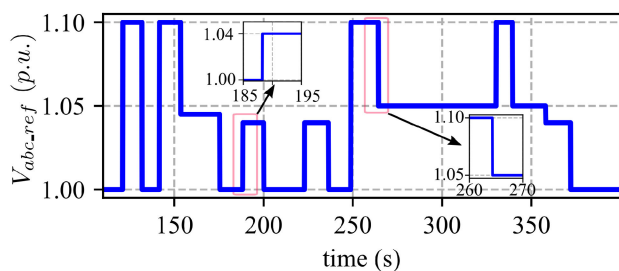

FIGURE 6. Step input given to actual system (SMA inverter). Several ranges of step input signals were provided, and the data were recorded. Focus only on the red rectangular box.

A. PARAMETERS SELECTION FOR DESIGNING PROBING SIGNAL

To determine the optimal parameters for a probing signal, the τ_{system} was evaluated by applying a step input to an inverter and observing the resulting output response. For this purpose, the Volt-Watt/Freq-Watt characteristic curves of the SMA inverter were set according to the IEEE 1547-2018 standard specified in Table 2. Initially, we will delve into the

TABLE 2. Load and SMA Inverter Parameters.

Parameter	Value
Resistive load	1 kW
SMA Rating	5 kW
Volt-Watt Setting	
P_1 and P_2	3, 0 and 0 kW resp.
V_1, V_2 and V_H	1.045, 1.085 and 1.095 p.u. resp.
Freq-Watt Setting	
P_1 and P_2	3, 0 and 0 kW resp.
F_1, F_2, and F_H	1.0083, 1.033, and 1.037 p.u. resp.

parameters needed to design the probing signal in Volt-Watt mode. The step input was given to the system to lay within the desired region (either R_1 or R_2), as indicated by the red rectangular box in Fig 6. For instance, the voltage input was changed from 1.0 to 1.04 p.u. in the case of R_1. The voltages within these ranges do not activate the voltage-active power function or the Volt-Watt mode as V_1 was set at 1.045 p.u. Similarly, the voltage input was changed from 1.1 to 1.05 p.u. in the case of R_2, as the voltage within these ranges activates the Volt-Watt mode of an SMA inverter.
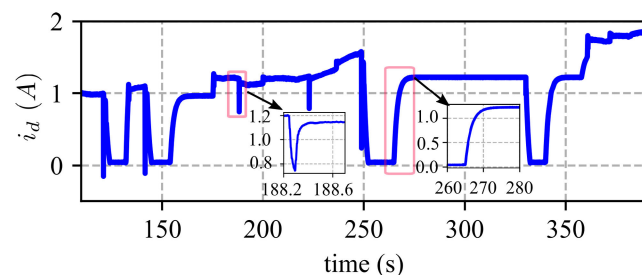

FIGURE 7. Corresponding response from SMA inverter after giving step input in the form of (Fig. 6).

When the Volt-Watt mode of an inverter is activated, the direct-axis current (i_d (A)) injected by the inverter is recorded and is depicted in Fig. 7. The voltage was changed from 1.0 to 1.04 p.u., where i_d (A) requires ($188.6\,s - 188.2\,s = 0.4\,s$) to settle to its steady-state value. This time was considered as a t_s, and τ of R_1 was calculated as 0.1 s. Similarly, the voltage was changed from 1.1 p.u. to 1.05 p.u., where the inverter i_d (A) response requires ($272\,s - 265\,s = 7\,s$) to settle to its steady-state value. This time was considered a t_s, and the τ of R_2 was calculated as 1.75 s.

To ensure coverage of the entire operational range with a single designed probing signal, the maximum and minimum frequency of the chirp signal were determined based on the smallest and largest τ between R_1 and R_2, respectively.

Hence, the logarithmic square chirp signal, f_0 and f_1, were taken as 0.5 Hz and 5 Hz, respectively. Due to the buffer size constraints imposed on the OP5707 RTDS, D of a chirp was taken as 5%, and T of the logarithmic square chirp signal was calculated as 15 s. The same approach was used to calculate the f_0 and f_1 of the chirp signal required to perturb an inverter while activating Freq-Watt mode. However, the frequencies designed for the Volt-Watt mode probing signal

TABLE 3. Parameters of sq-chirp signal for Volt-Watt and Freq-Watt modes of operation under IEEE 1547-2018 standards.

Operating Mode	Voltage/Frequency Amplitude Variation (p.u.)	Step Change (p.u.)	Frequency (Hz)
Volt-Watt	1 - 1.095	0.01	0.5-5
Freq-Watt	1-1.037	0.001	0.5-5

can be applied in the context of Freq-Watt mode, as the probing signal frequencies for Freq-Watt mode fall within the range of 0.5 to 5 Hz.

The voltage amplitude of the logarithmic square chirp probing signal was increased from 1 p.u. to 1.01 p.u. for 15 seconds, then was further increased by 0.005 p.u. until it reached 1.095 p.u. while the Volt-Watt mode was activated. A step-change of 0.01 p.u. was used based on the available voltage range in the Volt-Watt mode. Lowering the amplitude below 0.01 introduced noise, which can be removed by using a bandpass filter. It is important to note that the frequency was kept constant at 1 p.u. while the Volt-Watt mode was activated.

Moreover, the frequency amplitude of the logarithmic square chirp probing signal was changed from 1 p.u. to 1.001 p.u. for 15 s. The frequency amplitude was then increased by 0.0015 p.u. for the following range until it reached 1.0370 p.u. while activating Freq-Watt mode. Based on the availability of the frequency range (60 - 62 Hz) in the Freq-Watt mode, a 0.001 p.u. step-change was used. While analyzing the Freq-Watt mode, lowering the amplitude below 0.01 results in noisy output measurement; thus, a bandstop filter was used to eliminate the noise. Similarly, the voltage amplitude remains constant at 1 p. u. while activating the Freq-Watt mode. Table 3 shows the probing signals parameters used to perturb the voltage and frequency at PCC while activating the Volt-Watt and Freq-Watt modes, respectively.

IV. RESULTS AND ANALYSIS

The impact of varying irradiance in the dynamics model was analyzed with an experiment carried out over three contrasting irradiance level conditions: morning (around 10 a.m.), mid-day (around 2 p.m.), and evening (around 5 p.m.). The input, output, and irradiance datasets were logged for further analysis. The second-order TF was utilized to represent the overall dynamics of the SMA inverter using the logged input and output data set as it satisfies both accuracy and computing complexity requirements [54]. Due to the sporadic irradiance, the mean value of the irradiance data was considered. When the Volt-Watt mode of an inverter was activated, the mean value of the irradiance collected over 400 s during morning, mid-day, and evening were approximately 600, 980, and 520 W/m^2, respectively. Similarly, another day was considered while activating Freq-Watt mode, where the mean value of the irradiance level collected over 500 s in the morning, mid-day, and evening were approximately 310, 460, and 260 W/m^2, respectively.
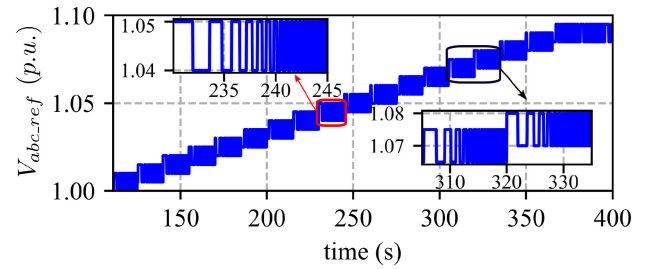

FIGURE 8. Logarithmic square chirp signal used to perturb the voltage at PCC.

The NRMSE technique was utilized to validate the obtained TF.

A. CASE-I: VOLT-WATT MODE

During three contrasting irradiance level conditions, the voltage amplitude at PCC was perturbed using the logarithmic square chirp signal (Fig. 8), which varies the voltage amplitude of PCC from 1 - 1.095 p.u., respectively. The actual response of the inverter (i_{invd}) after perturbation was noted and is depicted in Fig. 9 (a-c).
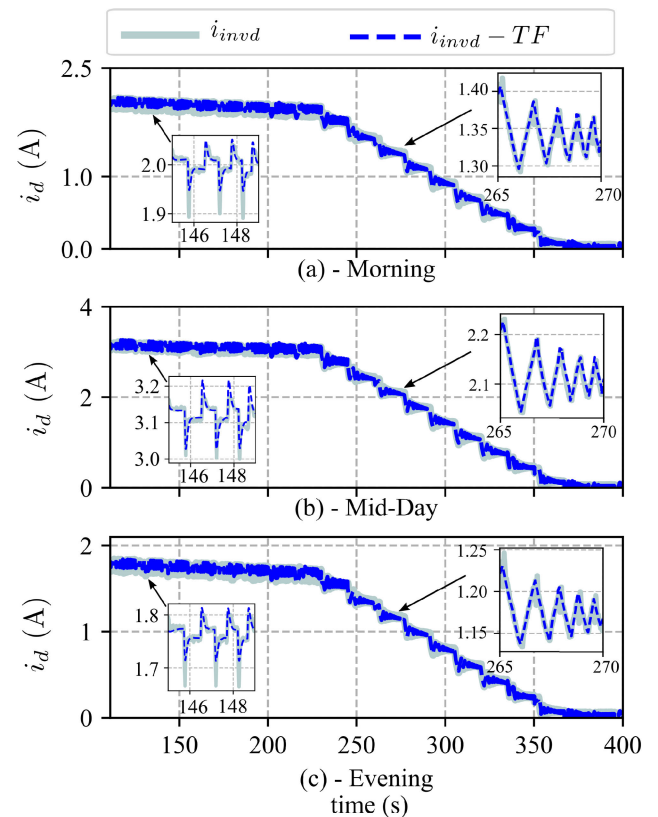

FIGURE 9. i_{invd} from (a)-(c) is the actual response of an inverter when perturbed by a logarithmic square chirp signal while activating Volt-Watt mode during three irradiance level conditions (i.e., morning, mid-day, and evening) and $i_{invd} - TF$ from (a)-(c) is the response of an SMA inverter when adjusted morning TF, mid-day TF, and adjusted evening TF are perturbed by logarithmic square signal respectively.

Partitioned modeling was employed to obtain the TF model of inverter dynamics, as explained in Section II-B. Based on the time length of the logarithmic square chirp signal, regions R_1, R_2, and R_3 datasets were divided into eight, nine, and three smaller ranges, respectively. The optimal separations of the range of region are based on the time length of the probing signal (15 s), the amplitude of the probing signal (0.01), and the step change (0.005). The mid-range data (r_{13}, r_{24}, and r_{31}) were used to obtain the TF of the respective regions. The analysis of region R_3 is not considered because the Volt-Watt mode of the SMA inverter was turned off, preventing the SMA from absorbing/injecting any active power in that region. The SysId algorithm was then developed, utilizing 70% of (V_{abc_ref} and its corresponding mid-day i_{invd}) as the input and output data, respectively, and the TF model of the inverter dynamics was obtained.
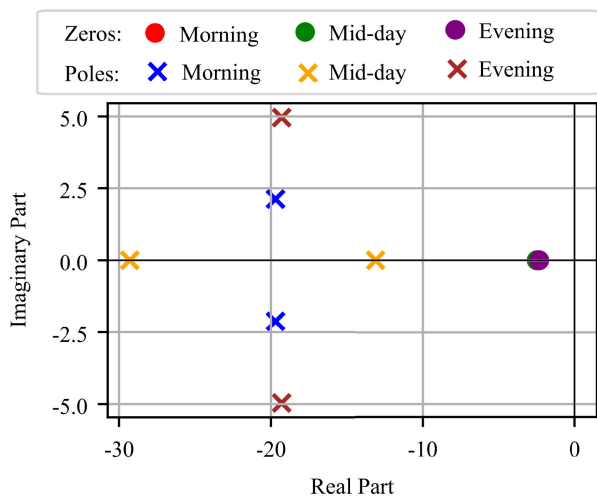

FIGURE 10. Pole-Zero Plot for Morning, Mid-day, and Evening TF of R_1.

The coefficient of the TF model of R_1 and R_2 during three contrasting irradiance level conditions is tabulated in Table 4. The estimated TF GOF was calculated and found within the acceptable limit ($\geq 90\%$) for each dynamic model.

The poles and zeros of the given transfer functions offer valuable insights into the system's behavior at different times of the day and their relationship with irradiance levels. For interpretation, the poles and zeros of R_1 are considered and are plotted in Fig. 10. Zeros at ≈ -2.35, -2.49, and -2.33 for the three irradiance levels indicate a consistent frequency at which the system output is zero throughout the day. Similarly, the fast and oscillatory response (poles at $-19.7 \pm 2.12j$) suggests the system quickly reacts to changes in irradiance, reflecting the dynamic nature of moderately high irradiance in the morning. The combination of fast and slower responses (poles at -29 and -13) indicates a more complex response, meaning the system manages high and relatively stable irradiance with a balanced response to both rapid and gradual changes during mid-day. Likewise, the fast and oscillatory response (poles at $-19.3 \pm 4.96j$) in the evening is similar to the morning but slightly slower. This slower response could reflect the diminishing light and
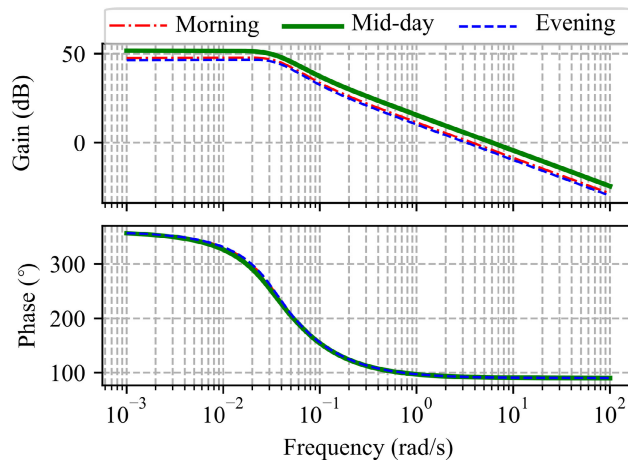

FIGURE 11. Bode response of TF model of R_2 obtained during three different periods of the day while activating Volt-Watt mode before adjusting the DC-gain in TF model of morning and evening.

TABLE 4. Summary of transfer function models of three time periods of the day while activating the Volt-Watt mode of the inverter.

Parts of Day	Model Coefficient of R_1	Model Coefficient of R_2
Morning	$b_1 = -300.1$ $b_0 = -706.2$ $a_2 = 1$ $a_1 = 39.4$ $a_0 = 392.6$	$b_1 = -26.42$ $b_0 = 11.47$ $a_2 = 1$ $a_1 = 0.2852$ $a_0 = 0.4805$
Mid-day	$b_1 = -347.6$ $b_0 = -866.1$ $a_2 = 1$ $a_1 = 42.4$ $a_0 = 383.9$	$b_1 = -37.69$ $b_0 = 16.96$ $a_2 = 1$ $a_1 = 0.3027$ $a_0 = 0.4382$
Evening	$b_1 = -295.9$ $b_0 = -690.2$ $a_2 = 1$ $a_1 = 38.60$ $a_0 = 397.1$	$b_1 = -20.35$ $b_0 = 10.11$ $a_2 = 1$ $a_1 = 0.2822$ $a_0 = 0.4897$

energy levels as evening approaches, necessitating a steadier system response. Similarly, the model coefficient of R_2 can be interpreted.

To avoid redundancy and focus primarily on the slope area illustrated in Fig. 1, the model of R_2 will be considered for further analysis. The Bode responses of the obtained TF of R_2 for the morning, mid-day, and evening scenarios are shown in Fig. 11. The Bode response indicates that dynamic models rely on different irradiance-level conditions as the gain of each model's Bode response does not coincide. Variations in irradiance can alter system behavior, affecting performance, model accuracy, control, and optimization. Accounting for these variations is crucial for accurate system understanding and control under different conditions. This paper excludes the Bode response of R_1. However, it follows a trend similar to that of R_2.

1) VALIDATION

The remaining 30% of the datasets were reserved for validation purposes. Initially, the data were inputted into individual TF representing morning, mid-day, and evening periods, and

the GOF was calculated, falling within acceptable bounds ($\geq$ 90% for each case). To validate the models further, we employed a mid-day model as a baseline and applied it to morning and evening irradiance conditions. However, adjustments were made to the models using a parameter denoted as K. The K value for each model was determined using Equation 6 (i.e., 6 (i.e., b_0/a_0)), resulting in values of -23.87, -38.71, and -20.65 for the morning, mid-day, and evening dynamic models, respectively. This adjustment involved scaling the morning and evening models relative to the mid-day model, leading to adjusted models for each period. The adjusted morning TF can be calculated as $\frac{\text{DC-gain of morning TF}}{\text{DC-gain of mid-day TF}} \times$ mid-day TF, whereas the mid-day TF will remain the same as we have taken mid-day TF as reference for scaling of morning and evening TF, and adjusted evening TF can be calculated as, adjusted evening TF = $\frac{\text{DC-gain of evening TF}}{\text{DC-gain of mid-day TF}} \times$ mid-day TF. The adjusted morning model will be ($\frac{-23.87}{-38.71}$) $\times$ mid-day TF and the adjusted evening model will be ($\frac{-20.65}{-38.71}$) $\times$ mid-day TF. These adjusted transfer functions were then used to analyze the corresponding morning, mid-day, and evening datasets. The resulting output responses are depicted in Fig. 9 (a-c) ($i_{invd}-TF$). GOF was then calculated, yielding values of 93.71% in the morning, 98.43% in the mid-day, and 94.53% in evening scenarios. This analysis suggests that the dynamic behavior of the inverter remains consistent throughout the day, although adjustments to the parameter K are necessary to account for variations in irradiance levels, indicating its dependence on irradiance.
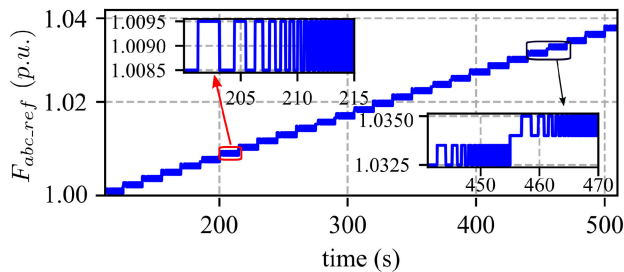

FIGURE 13. i_{invd} from (a)-(c) is the actual response of the inverter when perturbed by a logarithmic square chirp signal, $i_{invd} - Filt$ from (a)-(c) is the filtered response after incorporating band-stop filter and $i_{invd} - TF$ from (a)-(c) is the response of an SMA inverter when adjusted morning TF, mid-day TF and, adjusted evening TF, is perturbed by logarithmic square chirp signal respectively.

FIGURE 12. Logarithmic square chirp signal used to perturb the frequency at PCC.

B. CASE-II: FREQ-WATT MODE

Similar to Case-I, the setting of the Freq-Watt mode of the inverter was made accordingly to the Freq-Watt setting indicated in Table 2, and then the frequency at the PCC was perturbed using the logarithmic square chirp signal as a probing signal (Fig. 12) at three contrasting irradiance level condition.

The i_{invd} after perturbation was recorded and is shown in Fig. 13 (a-c). The response included noise due to limitations in the frequency range (60–62 Hz) and a low perturbation signal amplitude of 0.001 p.u. (0.6 Hz), failing signal-to-noise ratio criteria. A band-stop filter was designed to mitigate the noise, whose frequency is between 119 Hz and 123 Hz.
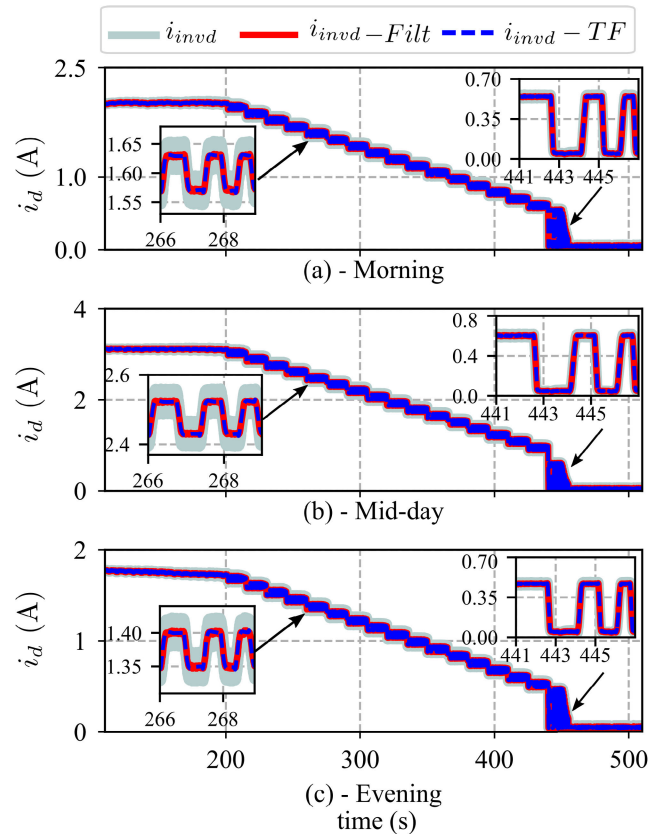
TABLE 5. Summary of transfer function models of three time periods of the day while activating Freq-Watt mode of inverter.

Parts of Day	Model Coefficient of R_2
Morning	$b_1 = 519.9$, $b_0 = -21970$, $a_2 = 1$, $a_1 = 28.71$, $a_0 = 365.6$
Mid-day	$b_1 = 1148$, $b_0 = -41690$, $a_2 = 1$, $a_1 = 32.54$, $a_0 = 458.2$
Evening	$b_1 = 452.4$, $b_0 = -18190$, $a_2 = 1$, $a_1 = 28.51$, $a_0 = 351.3$

The filtered response ($i_{invd} - Filt$) is shown in Fig. 13 (a-c) respectively.

To model inverter dynamics based on the frequency settings (listed in Table 2), regions R_1, R_2, and R_3 were divided into seven, ten, and two smaller ranges, respectively. In the case of the Freq-Watt mode, the analysis of regions R_1 and R_3 will be discarded, as the SMA inverter will prevent absorbing/injecting any active power in those regions.

A similar procedure, as explained in the Volt-Watt mode, was employed to obtain the TF model using mid-day, morning, and evening datasets. The model coefficients for each scenario are listed in Table 5. The Bode responses of the obtained TF of R_2 for the morning, mid-day, and evening irradiance scenarios are shown in Fig. 14. Bode's response showed that to make one model a generic model for
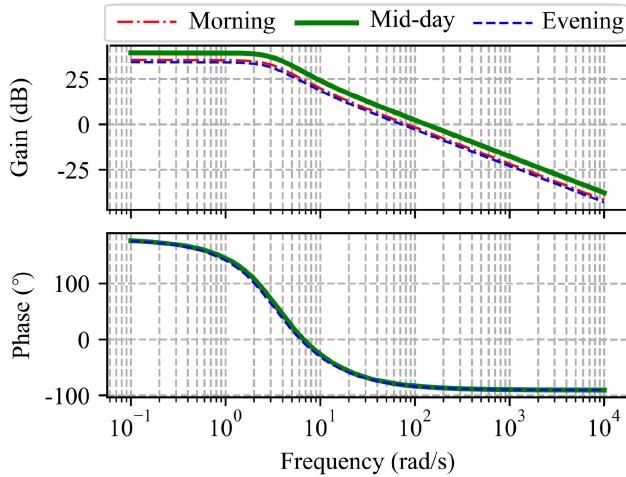
FIGURE 14. Bode response of TF model of R_2 obtained during three different periods of the day while activating Freq-Watt mode before adjusting the DC-gain in TF model of morning and evening.
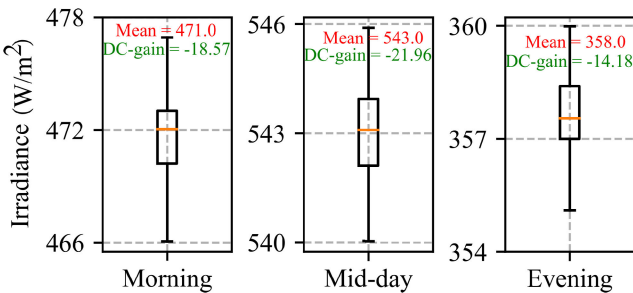

FIGURE 15. Variation of K of TF with irradiance while activating Volt-Watt mode.

contrasting irradiance level conditions, it has to undergo K adjustments.

After determining the K of each model, the mid-day model undergoes K adjustment, and the adjusted morning and evening TF was then determined, much like in Volt-Watt mode. The adjusted morning, mid-day, and evening TF feed the morning, mid-day, and evening data. The output responses are shown in Fig. 13 (a-c) ($i_{invd} - TF$). The GOF of R_2 was then calculated, which was 93.14% in the morning scenario, 95.34% in the mid-day scenario, and 91.32% in the evening scenario. This analysis also suggests that the dynamic behavior of the inverter remains consistent throughout the day, although adjustments to the parameter K are necessary to account for variations in irradiance levels, indicating its dependence on irradiance. Depending on the mode of activation of GSFs, the nature of dynamics varies. For instance, consider the Volt-Watt and Freq-Watt dynamics.

C. LINEAR DEPENDENCY OF DC-GAIN OF THE MODEL WITH IRRADIANCE

Our next step aimed to establish a relationship between the K of the model and irradiance, as irradiance can be easily measured using devices like a pyranometer. We observed the negative gradient linear relationship between the K of the model and irradiance mean.
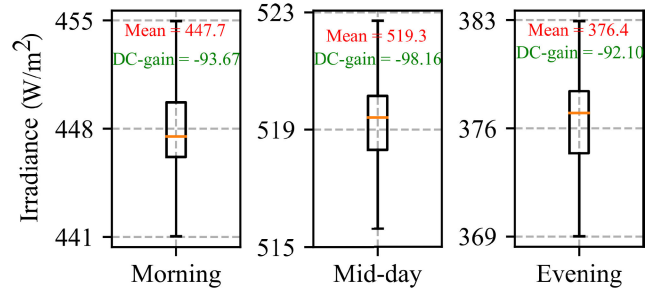

FIGURE 16. Variation of K of TF with irradiance while activating Freq-Watt mode.

For further verification, the input, output, and irradiance data at three periods of the day (these days considered are different from those of result and analysis) were logged on while activating the Volt-Watt and Freq-Watt modes. As the experiment was carried out under relatively stable irradiance conditions—with fluctuations limited to a narrow range compared to the larger variations observed on cloudy days and the mean value of irradiance was computed and a box plot of irradiance was plotted as depicted in Fig. 15 and Fig. 16 respectively. The data-driven model parametrization in new input and output datasets obtains the model. The new K of each of the models was computed for each mean irradiance level and is shown in Fig. 15 and Fig. 16 respectively. By analyzing the average irradiance and the corresponding K value of the model at that time, it can be concluded that K increases as irradiance increases and decreases as irradiance decreases. This observation is consistent whether activating the Volt-Watt or Freq-Watt mode.

We attempted to correlate the average irradiance level with the K of the model obtained at that time while activating the Freq-Watt or Volt-Watt mode. For each scenario-morning, mid-day, and evening-the K of the model showed a consistent negative gradient relationship with the mean irradiance level. i.e.,

$$K = -\frac{1}{B} \times \text{Irradiance}$$

Here, B is a gradient variable that links K to the mean irradiance. B is calculated based on the computed K and mean irradiance for mid-day, morning, and evening, and remains consistent for each period despite varying irradiance and K values. For example, in Fig. 15, the morning mean irradiance is 471.0 W/m^2 and K is -18.57, yielding a ratio of approximately -25. Similarly, during mid-day, the irradiance is 543.0 W/m^2 and K is -21.96, with a ratio of approximately -25. In the evening, the mean irradiance is 358.0 W/m^2 and K is -14.18, resulting in a ratio of about -25. For the inverter under test, B is 25 when activating the Volt-Watt mode, and 5 when activating the Freq-Watt mode. This analysis concludes that K for each model has a negative gradient linear relationship with irradiance, depending on the activation mode. However, the gradient value may vary depending on the manufacturer, which will be explored in future research.

V. CONCLUSION

This paper outlines a method for developing a dynamic model of COTS inverters through real-time digital experimentation, focusing on Volt-Watt and Freq-Watt modes. It details the creation of probing signals for perturbing the inverter and examines dynamic variations across different GSFs at various irradiance levels. The results indicate that while the dynamics remain consistent throughout the day, activation of different modes results in distinct dynamic adaptations, with the magnitude of dynamics varying based on irradiance conditions. Data-driven modeling was used to develop dynamic models under three distinct irradiance conditions, with each model achieving a GOF greater than 90%. The peak irradiance model (mid-day model) for Volt-Watt mode was successfully scaled to match morning and evening data, yielding GOF values of 93.71% and 94.53%, respectively. Similarly, the peak irradiance model for Freq-Watt mode was scaled to fit morning and evening data, achieving GOF values of 93.14% and 91.32%. This scaling was accomplished by adjusting the DC gain of the mid-day model. As the experiment was conducted under relatively stable irradiance conditions-with fluctuations limited to a narrow range compared to the larger variations observed on cloudy days—we analyzed the relationship between the DC-gain of each model and the average irradiance at the time of measurement. The findings showed that the DC-gain has a negative gradient correlation with mean irradiance, with different gradient values for the Volt-Watt and Freq-Watt modes. In conclusion, while a generic model can be developed, the DC-gain of this model must be adjusted according to the irradiance level. These models are valuable for simulation studies, stability analysis, control design, optimization, parameter estimation, and fault analysis. Future research may investigate variations in these negative gradients across different inverter models and manufacturers. This study initially used a purely resistive load for its simplicity and predictability—avoiding the complexities of inductance—future analysis will incorporate both resistive and inductive load systems to better reflect practical conditions and will concentrate on multi-input, multi-output scenarios, which involve the simultaneous activation of multiple GSFs and the perturbation of multiple variables.

VI. DATA AVAILABILITY

Data are available at [55], which is open source.

REFERENCES

[1] D. A. Kez, A. M. Foley, F. W. Ahmed, M. O'Malley, and S. M. Muyeen, "Potential of data centers for fast frequency response services in synchronously isolated power systems," *Renew. Sustain. Energy Rev.*, vol. 151, Nov. 2021, Art. no. 111547.

[2] *Real-Time Course of the Grid Frequency*. Accessed: Mar. 18, 2023. [Online]. Available: https://gridradar.net/de/netzfrequenz

[3] *IEEE Standard for Interconnection and Interoperability of Distributed Energy Resources With Associated Electric Power Systems Interfaces*, IEEE Standard 1547-2018, 2018, pp. 1–138.

[4] N. Ninad, E. Desjardins-Couture, and E. Apablaza-Arancibia, "Validating IEEE 1547 capabilities of DER inverter model using a real-time simulated inverter laboratory testbed," in *Proc. IEEE 10th Int. Conf. Smart Energy Grid Eng. (SEGE)*, Aug. 2022, pp. 105–110.

[5] O. Nelles, *Nonlinear System Identification: From Classical Approaches to Neural Networks, Fuzzy Models and Gaussian Processes*. Cham, Switzerland: Springer, 2021.

[6] S. Subedi, R. Fourney, H. M. Rekabdarkolaee, R. Tonkoski, T. M. Hansen, J. D. Vasquez-Plaza, and F. Andrade, "Impact of PLL design on data-driven models for grid-connected single-phase inverters," in *Proc. Int. Symp. Power Electron., Electr. Drives, Autom. Motion (SPEEDAM)*, Jun. 2022, pp. 930–935.

[7] I. Staffell. (Apr. 2021). *Britain's Blackout*. [Online]. Available: https://www.drax.com/opinion/britains-blackout/#chapter-1

[8] R. Yan, N.-A. Masood, T. K. Saha, F. Bai, and H. Gu, "The anatomy of the 2016 South Australia blackout: A catastrophic event in a high renewable network," *IEEE Trans. Power Syst.*, vol. 33, no. 5, pp. 5374–5388, Sep. 2018.

[9] R. Chakraborty, H. Jain, and G.-S. Seo, "A review of active probing-based system identification techniques with applications in power systems," *Int. J. Electr. Power Energy Syst.*, vol. 140, Sep. 2022, Art. no. 108008.

[10] L. Ljung, *System Identification: Theory for the User*. Upper Saddle River, NJ, USA: Prentice-Hall, 2012.

[11] H. D. Abbood and A. Benigni, "Data-driven modeling of a commercial photovoltaic microinverter," *Model. Simul. Eng.*, vol. 2018, pp. 1–11, Apr. 2018.

[12] C. Shah, J. D. Vasquez-Plaza, D. D. Campo-Ossa, J. F. Patarroyo-Montenegro, N. Guruwacharya, N. Bhujel, R. D. Trevizan, F. A. Rengifo, M. Shirazi, R. Tonkoski, R. Wies, T. M. Hansen, and P. Cicilio, "Review of dynamic and transient modeling of power electronic converters for converter dominated power systems," *IEEE Access*, vol. 9, pp. 82094–82117, 2021.

[13] P. Gupta, V. Pahwa, and Y. P. Verma, "Switching function based inverter modeling for a grid-connected SOFC system in real time," *IOP Conf. Ser., Mater. Sci. Eng.*, vol. 1033, no. 1, Jan. 2021, Art. no. 012023, doi: 10.1088/1757-899X/1033/1/012023.

[14] B. Hammer, K. Gong, and U. Konigorski, "Modeling and control of inverter-based microgrids," *IFAC-PapersOnLine*, vol. 51, no. 2, pp. 19–24, 2018. [Online]. Available: https://www.sciencedirect.com/science/article/pii/S2405896318300041

[15] P. K. Sahu, P. Shaw, and S. Maity, "Modeling and control of grid-connected DC/AC converters for single-phase micro-inverter application," in *Proc. Annu. IEEE India Conf. (INDICON)*, Dec. 2015, pp. 1–6.

[16] A. Nagarajan and R. Ayyanar, "Dynamic phasor model of single-phase inverters for analysis and simulation of large power distribution systems," in *Proc. 4th IEEE Int. Symp. Power Electron. Distrib. Gener. Syst. (PEDG)*, Jul. 2013, pp. 1–6.

[17] Z. Li, Y. Gao, X. Zhang, B. Wang, and H. Ma, "A model-data-hybrid-driven diagnosis method for open-switch faults in power converters," *IEEE Trans. Power Electron.*, vol. 36, no. 5, pp. 4965–4970, May 2021.

[18] S. Lu, W. Gu, S. Ding, S. Yao, H. Lu, and X. Yuan, "Data-driven aggregate thermal dynamic model for buildings: A regression approach," *IEEE Trans. Smart Grid*, vol. 13, no. 1, pp. 227–242, Jan. 2022.

[19] S. Subedi, J. D. Vasquez-Plaza, F. Andrade, H. M. Rekabdarkolaee, R. Fourney, R. Tonkoski, and T. M. Hansen, "Aggregate data-driven dynamic modeling of active distribution networks with DERs for voltage stability studies," *IET Renew. Power Gener.*, vol. 18, no. 14, p. 2261–2276, Jul. 2024.

[20] P. C. Krause, O. Wasynczuk, and S. D. Sudhoff, *Analysis of Electric Machinery and Drive Systems*, vol. 7. Hoboken, NJ, USA: Wiley, 2013.

[21] C.-J. Lin, A. Y.-T. Chen, C.-Y. Chiou, C.-H. Huang, H.-D. Chiang, J.-C. Wang, and L. Fekih-Ahmed, "Dynamic load models in power systems using the measurement approach," *IEEE Trans. Power Syst.*, vol. 8, no. 1, pp. 309–315, Feb. 1993.

[22] J. J. Sanchez-Gasca and J. H. Chow, "Computation of power system low-order models from time domain simulations using a Hankel matrix," *IEEE Trans. Power Syst.*, vol. 12, no. 4, pp. 1461–1467, Nov. 1997.

[23] L. Fan and Z. Miao, "Admittance-based stability analysis: Bode plots, Nyquist diagrams or eigenvalue analysis?" *IEEE Trans. Power Syst.*, vol. 35, no. 4, pp. 3312–3315, Jul. 2020.

[24] N. B. Erichson, L. Mathelin, J. N. Kutz, and S. L. Brunton, "Randomized dynamic mode decomposition," *SIAM J. Appl. Dyn. Syst.*, vol. 18, no. 4, pp. 1867–1891, Jan. 2019, doi: 10.1137/18M1215013.

[25] A. Almunif, L. Fan, and Z. Miao, "A tutorial on data-driven eigenvalue identification: Prony analysis, matrix pencil, and eigensystem realization algorithm," *Int. Trans. Electr. Energy Syst.*, vol. 30, no. 4, Apr. 2020, Art. no. e12283.

[26] N. Guruwacharya, N. Bhujel, U. Tamrakar, M. Rauniyar, S. Subedi, S. E. Berg, T. M. Hansen, and R. Tonkoski, "Data-driven power electronic converter modeling for low inertia power system dynamic studies," in *Proc. IEEE Power Energy Soc. Gen. Meeting (PESGM)*, Aug. 2020, pp. 1–5.

[27] N. Guruwacharya, S. Chakraborty, G. Saraswat, R. Bryce, T. M. Hansen, and R. Tonkoski, "Data-driven modeling of grid-forming inverter dynamics using power hardware-in-the-loop experimentation," *IEEE Access*, vol. 12, pp. 52267–52281, 2024.

[28] B. Poudel. *Dynamic Modeling of Commercial-Off-The-Shelf Smart Inverters Using Power-Hardware-in-the-Loop*. Accessed: 2023. [Online]. Available: https://openprairie.sdstate.edu/etd2/701/

[29] N. Guruwacharya, "Probing signal-based data-driven modeling of power electronics smart converter dynamics using power hardware-in-the-loop," Ph.D. dissertation, Dept. Elect. Eng. Comput. Sci., South Dakota State Univ., 2023.

[30] J. W. Pierre, N. Zhou, F. K. Tuffner, J. F. Hauer, D. J. Trudnowski, and W. A. Mittelstadt, "Probing signal design for power system identification," *IEEE Trans. Power Syst.*, vol. 25, no. 2, pp. 835–843, May 2010.

[31] J. Zhang, C. Lu, and Y. Han, "MIMO identification of power system with low level probing tests: Applicability comparison of subspace methods," *IEEE Trans. Power Syst.*, vol. 28, no. 3, pp. 2907–2917, Aug. 2013.

[32] A. Cabrera-Tobar, E. Bullich-Massagué, M. Aragüés-Peñalba, and O. Gomis-Bellmunt, "Capability curve analysis of photovoltaic generation systems," *Sol. Energy*, vol. 140, pp. 255–264, Dec. 2016. [Online]. Available: https://www.sciencedirect.com/science/article/pii/S0038092X16305291

[33] L. Feng, F. U. Hamelmann, J. Zhang, K. Ding, M. Diehl, T. Pfeil, S. Brandt, W. Friedrich, and N. Amin, "A novel method to evaluate irradiance in PV field without irradiance sensors," in *Proc. 47th IEEE Photovoltaic Spec. Conf. (PVSC)*, Jun. 2020, pp. 2496–2501.

[34] A. Cabrera-Tobar, E. Bullich-Massagué, M. Aragüés-Peñalba, and O. Gomis-Bellmunt, "Active and reactive power control of a PV generator for grid code compliance," *Energies*, vol. 12, no. 20, p. 3872, Oct. 2019.

[35] V. M. R. de Jesus, A. F. Cupertino, L. S. Xavier, H. A. Pereira, and V. F. Mendes, "Operation limits of grid-tied photovoltaic inverters with harmonic current compensation based on capability curves," *IEEE Trans. Energy Convers.*, vol. 36, no. 3, pp. 2088–2098, Sep. 2021.

[36] K. A. Kim, C. Xu, L. Jin, and P. T. Krein, "A dynamic photovoltaic model incorporating capacitive and reverse-bias characteristics," *IEEE J. Photovolt.*, vol. 3, no. 4, pp. 1334–1341, Oct. 2013.

[37] E. Scolari, F. Sossan, and M. Paolone, "Photovoltaic-model-based solar irradiance estimators: Performance comparison and application to maximum power forecasting," *IEEE Trans. Sustain. Energy*, vol. 9, no. 1, pp. 35–44, Jan. 2018.

[38] A. Asgharzadeh, M. A. Anoma, A. Hoffman, C. Chaudhari, S. Bapat, R. Perkins, D. Cohen, G. M. Kimball, D. Riley, F. Toor, and B. Bourne, "A benchmark and validation of bifacial PV irradiance models," in *Proc. IEEE 46th Photovoltaic Spec. Conf. (PVSC)*, Jun. 2019, pp. 3281–3287.

[39] J. F. Gaviria, G. Narváez, C. Guillen, L. F. Giraldo, and M. Bressan, "Machine learning in photovoltaic systems: A review," *Renew. Energy*, vol. 196, pp. 298–318, Aug. 2022. [Online]. Available: https://www.sciencedirect.com/science/article/pii/S0960148122009454

[40] B. E. Hefni, "Dynamic modeling of concentrated solar power plants with the ThermoSysPro library (Parabolic trough collectors, Fresnel reflector and solar-hybrid)," *Energy Proc.*, vol. 49, pp. 1127–1137, Jan. 2014. [Online]. Available: https://www.sciencedirect.com/science/article/pii/S1876610214005761

[41] F. Shaik, B. Maheswari, G. N. Anitha, D. Charitha, M. K. Kumar, and B. V. S. Thrinath, "An assessment of power regulation strategy and fuzzy controller for a grid-interfaced solar photovoltaic system," in *Proc. 4th Int. Conf. Pervasive Comput. Social Netw. (ICPCSN)*, May 2024, pp. 831–836.

[42] S. Subedi, B. Poudel, P. Aslami, R. Fourney, H. M. Rekabdarkolaee, R. Tonkoski, and T. M. Hansen, "Automated data–driven model extraction and validation of inverter dynamics with grid support function," *e-Prime-Adv. Electr. Eng., Electron. Energy*, vol. 6, Dec. 2023, Art. no. 100365.

[43] N. Guruwacharya, N. Bhujel, T. M. Hansen, S. Suryanarayanan, R. Tonkoski, U. Tamrakar, and F. Wilches-Bernal, "Modeling inverters with grid support functions for power system dynamics studies," in *Proc. IEEE Power Energy Soc. Innov. Smart Grid Technol. Conf. (ISGT)*, Feb. 2021, pp. 1–5.

[44] S. Subedi, N. Guruwacharya, R. Fourney, H. M. Rekabdarkolaee, R. Tonkoski, T. M. Hansen, U. Tamrakar, and P. Cicilio, "Computationally efficient partitioned modeling of inverter dynamics with grid support functions," in *Proc. 47th Annu. Conf. IEEE Ind. Electron. Soc. (IECON)*, Oct. 2021, pp. 1–6.

[45] *System Identification Toolbox*. Accessed: Oct. 31, 2019. [Online]. Available: https://www.mathSMAworks.com/help/ident/ref/compare.html

[46] A. Brosch, S. Hanke, O. Wallscheid, and J. Böcker, "Data-driven recursive least squares estimation for model predictive current control of permanent magnet synchronous motors," *IEEE Trans. Power Electron.*, vol. 36, no. 2, pp. 2179–2190, Feb. 2021.

[47] B. Poudel, P. Aslami, T. Aryal, N. Bhujel, A. Rai, M. Rauniyar, H. M. Rekabdarkolaee, U. Tamrakar, T. M. Hansen, and R. Tonkoski, "Comparative analysis of state and parameter estimation techniques for power system frequency dynamics," in *Proc. Int. Symp. Power Electron., Electr. Drives, Autom. Motion (SPEEDAM)*, Jun. 2022, pp. 754–761.

[48] A. H. Tan and K. R. Godfrey, *Industrial Process Identification: Perturbation Signal Design and Applications*. Cham, Switzerland: Springer, 2019.

[49] *Time Domain Specifications*. Accessed: 2023. [Online]. Available: https://www.tutorialspoint.com/control_systems/control_systems_time_domain_specifications.htm

[50] B. Poudel, M. Panwar, and R. Hovsapian, "Dynamic response verification of vector controlled induction machines for hydropower emulation," in *Proc. IEEE Kansas Power Energy Conf. (KPEC)*, Apr. 2024, pp. 1–5.

[51] A. Novak, L. Simon, F. Kadlec, and P. Lotton, "Nonlinear system identification using exponential swept-sine signal," *IEEE Trans. Instrum. Meas.*, vol. 59, no. 8, pp. 2220–2229, Aug. 2010.

[52] *How to Find The DC Gain of a Transfer Function (Examples Included)*. Electrical 4 U. Accessed: May 29, 2024. [Online]. Available: https://www.electrical4u.com/dc-gain-transfer-function/

[53] *Technical Information of Grid Support Utility Interactive Inverters Sunny Boy*. Accessed: Jan. 3, 2017. [Online]. Available: https://files.sma.de/downloads/SBxx-1XP-US-40-GridServices-TI-en-15.pdf

[54] N. Guruwacharya, H. Bhandari, S. Subedi, J. D. Vasquez-Plaza, M. L. Stoel, U. Tamrakar, F. Wilches-Bernal, F. Andrade, T. M. Hansen, and R. Tonkoski, "Data-driven modeling of commercial photovoltaic inverter dynamics using power hardware-in-the-Loop," in *Proc. Int. Symp. Power Electron., Electr. Drives, Autom. Motion (SPEEDAM)*, Jun. 2022, pp. 924–929.

[55] S. Subedi, N. Guruwacharya, B. Poudel, J. D. Vasquez-Plaza, F. Andrade, R. Fourney, H. M. Rekabdarkolaee, T. M. Hansen, and R. Tonkoski, "Leveraging data-driven models for accurate analysis of grid-tied smart inverters dynamics," 2023, *arXiv:2310.02056*.

BIDUR POUDEL (Member, IEEE) received the bachelor's degree in electrical engineering from the Institute of Engineering, Tribhuvan University, Kathmandu, Nepal, in 2019, and the M.S. degree in electrical engineering from South Dakota State University (SDSU), Brookings, SD, USA, in 2023. He is currently a Research Engineer II with the National Renewable Energy Laboratory. His research interests include power system modeling and simulation, microgrid viability analysis, hydro-technologies analysis, optimal control, estimation in microgrids, and dynamic studies.

NISCHAL GURUWACHARYA (Member, IEEE) received the B.E. degree in electrical engineering and the M.Sc. degree in energy systems planning and management from Tribhuvan University, Nepal, in 2013 and 2019, respectively, and the Ph.D. degree in electrical engineering from South Dakota State University, Brookings, SD, USA. Currently, he is a Researcher with the National Renewable Energy Laboratory. His research interests include data-driven modeling of power electronics converters, power electronics and control, power hardware-in-the-loop, and grid integration of renewable energy systems.

SUNIL SUBEDI (Member, IEEE) received the B.Eng. degree in electrical engineering from the Institute of Engineering, Tribhuvan University, Kathmandu, Nepal, in 2018, and the Ph.D. degree in electrical engineering from South Dakota State University, Brookings, SD, USA, in 2023. He was a Graduate III Electrical Engineering Intern with the National Renewable Energy Laboratory, Golden, CO, USA, from May 2022 to December 2022, where he worked on projects related to the grid integration of grid-supportive loads and distributed energy resources. He is currently a Postdoctoral Research Associate with Oak Ridge National Laboratory, Oak Ridge, TN, USA. His research interests include grid integration of renewable energy systems, power system dynamic modeling, simulation, stability, application of machine learning in power systems, and power electronic converters.

UJJWOL TAMRAKAR (Member, IEEE) received the B.E. degree in electrical engineering from Tribhuvan University, Nepal, in 2011, and the M.S. and Ph.D. degrees in electrical engineering from South Dakota State University (SDSU), Brookings, SD, USA, in 2015 and 2020, respectively. He is currently a Senior Research and Development Engineer at Sandia National Laboratories, Albuquerque, NM, USA. His research interests include grid integration of renewable energy systems, energy storage analytics, power system modeling and stability, and optimal control. He has been actively involved in various IEEE task forces related to voltage and frequency stability of power systems with high renewable penetration. He serves as an Editor for IEEE Open Access Journal of Power and Energy and IEEE Access.

FELIPE WILCHES-BERNAL (Senior Member, IEEE) received the M.S. degree in control systems and signal processing from the Université Paris-Sud XI, Orsay, France, and the Ph.D. degree in electrical engineering from the Rensselaer Polytechnic Institute, Troy, NY, USA. He joined the Electric Power Systems Research Department, Sandia National Laboratories, Albuquerque, NM, USA, in 2015, where he was a Principal Member of the Technical Staff. Since joining Sandia, he was a Key Technical Contributor and a PI/Co-PI of multiple projects in the power systems integration area. His research interests include power system stability and control, renewable energy and smart grid technologies, and signal processing and control techniques applied to power systems. He was a Key Contributor to the team that received the 2017 Research and Development 100 Award, for developing a control system for active damping of inter-area oscillations.
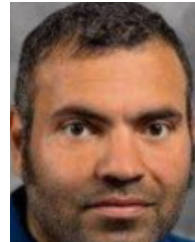
HOSSEIN MORADI REKABDARKOLAEE (Senior Member, IEEE) received the B.S. degree in statistics from the University of Mazandaran, Mazandaran, Iran, in 2008, the M.S. degree in mathematical statistics from Tarbiat Modares University, Tehran, Iran, in 2012, and the M.S. degree in mathematics with concentration in operations research and the Ph.D. degree in systems modeling and analysis from Virginia Commonwealth University, Richmond, VA, USA, in 2014 and 2016, respectively. He is currently an Assistant Professor with the Department of Mathematics and Statistics, South Dakota State University, Brookings, SD, USA. His research interests include developing statistical models for spatial and spatiotemporal data, functional data, and multivariate data for making inferences from massive datasets, all motivated by the desire to tackle scientific problems. He is an Active Member of the American Statistical Association (ASA) and the International Society of Bayesian Analysis (ISBA). He was a recipient of the 2019 Best Faculty Poster Presentation Award at the SRCOS Summer Conference, the 2015 and 2016 Best Oral Presentation Award at Virginia Academy of Science, and the 2015 Best Poster Award at the Psychiatric Society of Virginia Fall Conference. He served as a member for the ENVR-Student Paper AWARD, Joint Statistical Meeting, 2018–2020 (the chair of the committee, in 2020).

TIMOTHY M. HANSEN (Senior Member, IEEE) received the B.S. degree in computer engineering from Milwaukee School of Engineering, Milwaukee, WI, USA, in 2011, and the Ph.D. degree in electrical engineering from Colorado State University, Fort Collins, CO, USA, in 2015.

He is currently the Harold C. Hohbach Endowed Associate Professor with the Electrical Engineering and Computer Science Department, South Dakota State University, Brookings, SD, USA. His research interests include optimization, high-performance computing, electricity market applications to sustainable power and energy systems, converter-dominated power systems, and cyber-physical-social systems.

REINALDO TONKOSKI (Senior Member, IEEE) received the B.A.Sc. degree in control and automation engineering and the M.Sc. degree in electrical engineering from the Pontificia Universidade Católica do RS (PUC-RS), Brazil, in 2004 and 2006, respectively, and the Ph.D. degree from Concordia University, Canada, in 2011.

Currently, he is a Professor and the Chair of electric power transmission and distribution with the Technical University of Munich. He has authored over 100 technical publications in peer-reviewed journals and conferences. His research interests include grid integration of sustainable energy technologies, energy management, power electronics, and control systems. He is an Editor of IEEE Transactions on Sustainable Energy, IEEE Access, and IEEE Systems Journal.

• • •